Open Archive TOULOUSE Archive Ouverte (OATAO)
OATAO is an open access repository that collects the work of Toulouse researchers and makes it freely available over the web where possible.

This is a publisher-deposited version published in: http://oatao.univ-toulouse.fr/
Eprints ID: 15764

To link to this article: DOI: 10.1504/IJESMS.2016.075550
URL: http://dx.doi.org/10.1504/IJESMS.2016.075550

To cite this version: Bonnin, Vincent and Bénard, Emmanuel and Toomer, Christine and Moschetta, Jean-Marc *Dynamic soaring mechanisms in the ocean boundary layer*. (2016) International Journal of Engineering Systems Modelling and Simulation, vol. 8 (N° 2). pp. 136-148. ISSN 1755-9758

Any correspondence concerning this service should be sent to the repository administrator: staff-oatao@listes-diff.inp-toulouse.fr

Dynamic soaring mechanisms in the ocean boundary layer

Vincent Bonnin* and Emmanuel Benard

ISAE,
Université de Toulouse,
10 av. Edouard Belin, BP 54032,
31055 Toulouse Cedex 4, France
Email: vincent.bonnin@isae.fr
Email: emmanuel.benard@isae.fr
*Corresponding author

Christine A. Toomer

University of the West of England,
Bristol, England BS16 1QY, UK
Email: chris.toomer@uwe.ac.uk

Jean-Marc Moschetta

ISAE,
Université de Toulouse,
10 av. Edouard Belin, BP 54032,
31055 Toulouse Cedex 4, France
Email: jeanmarc.moschetta@isae.fr

Abstract: Dynamic soaring is a flying technique which extracts energy from an environment where wind gradients form, such as the air-sea interface above oceans that sees such gradients developing through multiple and combined phenomena. Models of wind-wave interactions are analysed in terms of their influence on the induced wind field, before selecting a purely sinusoidal peak wave from the wave spectrum and developing the related wind field using stable laminar theory. Dynamic soaring trajectories are then derived by optimising a nonlinear constrained problem that models the evolution of a point mass vehicle. Characteristic phases of dynamic soaring flight are evidenced out of the overall trajectories and compared to the flat-ocean case in order to conclude on the influence of waves regarding dynamic soaring performances.

Keywords: albatross; dynamic soaring; optimisation; UAV; wind gradient; idealised wave; wave soaring; ocean; boundary layer.

Reference to this paper should be made as follows: Bonnin, V., Benard, E., Toomer, C.A. and Moschetta, J-M. (2016) 'Dynamic soaring mechanisms in the ocean boundary layer', *Int. J. Engineering Systems Modelling and Simulation*, Vol. 8, No. 2, pp.136–148.

Biographical notes: Vincent Bonnin graduated from ENSMA in 2011 and is currently conducting his PhD between UWE, Bristol, UK and ISAE, Toulouse, as part of joint PhD agreement. His interests include dynamic soaring, UAVs, wind energy extraction, nonlinear optimisation, applied aerodynamics and biomimicry.

Emmanuel Benard received his MSc from University of Poitiers, France in 1991 and PhD in Aerodynamics. After lecturing experience in the UK, including the Queen's University of Belfast and the University of Glasgow, he joined ISAE, Toulouse, France where he is currently an Associate Professor in the Department of Aerodynamics Energetics and Propulsion. He is the Leader of the Advanced Aerodynamics and Flow Control research group and has years of experience in experimental fluid dynamics and unsteady aerodynamics.

Christine A. Toomer studied mathematics and physics at Imperial College, leading to a PhD award in 1986, for her work on stellar and terrestrial atmospheres. She then moved to industry to work on space vehicle propulsion and hypersonic vehicles. She has been employed at BAE Systems, NASA and universities in the UK and abroad and is currently a Principal Lecturer at the University of the West of England, Bristol, UK.

Copyright © 2016 Inderscience Enterprises Ltd.

Jean-Marc Moschetta is a Professor of Aerodynamics in the Department Aerodynamics, Energetics and Propulsion at ISAE, Toulouse, France. He graduated from SUPAERO in 1987 and was awarded a PhD in Fluid Mechanics in 1991. He is currently a Professor in the Department of Aerodynamics at ISAE, Toulouse, France and is the leader of the micro-UAV research axis.

This paper is a revised and expanded version of a paper entitled 'Dynamic soaring mechanisms in the ocean boundary layer' presented at the 49th Applied Aerodynamics Symposium, Lille, France, 24–26 March 2014.

1 Introduction

Dynamic soaring has first been observed from albatrosses, such as pictured in Figure 1, sustaining non-flapping flight at sea. It did not seem probable that a vertical motion of the air above the ocean surface could be high enough to maintain birds in flight. So Rayleigh (1883) analysed that a vertical variation in horizontal wind could enable the bird to maintain or increase its energy level by repeatedly flying through the zone of wind gradient. Those observations were completed much later by a 1990 satellite-tracking campaign (Jouventin and Weimerkirsch, 1990), which showed that albatrosses could fly up to 800 kilometers a day, shedding a new light on the subject of dynamic soaring flight.

Several studies aimed at analysing the inherent flight model of albatrosses (Idrac, 1925; Wood, 1925; Sachs, 2004) and dynamic soaring research gained momentum with developments in the domain of small-sized UAVs, where endurance is acknowledged to be a key utility factor (US Department of Defense, 2005). However, the nature of energy-harvesting mechanisms has been controversial and still suffers from a lack of consistency. Pennycuick (2002) uses his direct observations to claim that albatrosses gain their energy out of gusts created by flow separation over waves. Sachs (2004), Deittert et al. (2009) and Bonnin et al. (2013) showed through numerical studies that classic wind-shear soaring over a flat ocean surface can provide conditions for sustainable flight. Richardson (2011) describes how the different energy-extraction theories are not mutually exclusive but could rather be combined during dynamic soaring flight, although no further analysis supports this claim.

Those differences mainly arise from the fact that dynamic soaring research is faced with a significant limitation regarding the environment models considered. Although the ocean surface holds the significant advantage to be rather flat and uniform compared to earth landscape, the wind profiles encountered are not that of a flat plate. So far, the environment was only taken into account through steady boundary layer vertical wind profiles, either following power-law behaviour (Deittert et al., 2009; Bonnin et al., 2013), or logarithmic evolution (Sachs, 2004; Bower, 2011), or even a linear wind profile (Bower, 2004). However, those profiles are constant in space and time and are not correlated with any environment variable, apart from setting the reference wind itself. The purpose of this paper is to refine the environment model used in simulations so as to correlate the wind field with environment conditions and to describe how dynamic soaring could be affected by the presence of a moving wavy surface. The Charnock model (Fairall et al., 1996) will be considered for modelling the sea-surface roughness before selecting a peak sinusoidal wave from the Pierson-Moskowitz spectrum (Fairall, 1982) and using stable laminar flow theory to determine the resulting wind-field. Then, simulations will be conducted by transposing albatross characteristics to a point mass model. Results will be detailed with a particular emphasise on the influence of waves.

Figure 1 Wandering albatross in flight with wing tip feathers just touching the surface (see online version for colours)

2 Environment model

2.1 Wind profile over rather flat surfaces

In the present case of this study, we consider neutral conditions at sea, which means convective exchanges or heat transmission are absent. Those conditions are met whenever the surface is cooler than the air above. The subsequent boundary layer is therefore solely driven by wind shear turbulence and classical theory of the turbulent boundary layer can be used. A distinction between two cases is made: either the surface is considered smooth and therefore the mean velocity profile is that of a flat plate, or the roughness of the surface induces changes in the velocity

profile. Some concepts related to that theory are introduced hereafter. The friction velocity u_* is defined by equation (1) and is a representation of the stress τ_p exerted by the wind on the ocean surface. The air density is represented by ρ.

$$u_* = \sqrt{\frac{\tau_p}{\rho}} \tag{1}$$

The friction length z_* of the boundary layer is the length scale of the internal sub-layer and is related to the viscosity v by equation (2).

$$z_* = \frac{v}{u_*} \tag{2}$$

The general form of the dependence of the mean velocity profile $\bar{u}$ over a flat rigid wall, at a distance z, is called the *universal law of the wall* and is developed in equation (3).

$$\bar{u}(z) = u_* f\left(\frac{z}{z_*}\right) \tag{3}$$

The former relation is only valid for surfaces considered as dynamically smooth, that is to say when eventual protrusions on the surface are small enough not to entail a change in the mean velocity profile. Monin and Yaglom (187) propose a quantitative explanation of the requirement of the smoothness: the wall will be considered as dynamically smooth if the mean height h_0 of the protrusions satisfies the condition given by equation (4).

$$h_0 \leq z_* = \frac{v}{u_*} \tag{4}$$

In the ocean atmosphere, for friction velocity of the order of 10 cm/s, the friction length does not exceed some tenth of a millimetre and quite trivially the ocean surface cannot be considered as dynamically smooth. Therefore, the main velocity profile departs from the case of a flat surface and will depend on irregularities of the surface. Those are considered in the expression of the main wind profile, via the roughness length z_0, defined in equation (5), which is characteristic of the dynamic interaction between flow and surface (Monin and Yaglom, 1987).

$$z_0 = z \exp\left(\frac{-\chi\sqrt{2}}{\sqrt{C_f(z)}}\right) \tag{5}$$

C_f is the friction coefficient at the altitude z, and c is the von Karman constant. It should be noted that z_0 is constant whatever the value of z, given that the shear stress is almost constant within the boundary layer. The mean velocity profile over a rough surface is subsequently given in equation (6) (Monin and Yaglom, 1987).

$$\bar{u}(z) = \frac{u_*}{\chi}\log\left(\frac{z}{z_0}\right) \tag{6}$$

There is a one to one correspondence between the state of the surface, with a set of protrusions h_0 irregularly spaced and the roughness length z_0.

Earlier dynamic soaring studies, such as Wood (1925), Sachs (2004), Barate et al. (2006) and Bower (2011), use and mention values of z_0 around 3 cm, which is supposed to represent a typical value over *very rough seas*. They implicitly assume that ocean surface irregularities are of the order of the metre, which seems a priori fair for rugged conditions at sea. However, several limitations are going against the use of this estimation of z_0 for defining the mean wind velocity profile in the present case of dynamic soaring over oceans.

The first limitation is that specific literature on the topic refers to significant lower values. Stull (1994) mentions values for z_0 of the order of the millimetre for *off-sea wind in coastal areas*, while all existing data indicate that the surface of the sea is considerably smoother than the majority of land surfaces, with $z_0 < 1$ mm even for a fairly strong wind.

Moreover, the velocity profile defined in equation (6) accounts for irregularities from the surface only in a statistical way. Although that velocity profile is mathematically defined down to z_0, in fact the logarithmic equation loses its physical consistence at much higher altitude. Indeed, for altitudes to the order of the height h_0 of protrusions on the surface, the velocity profile would vary depending on the shape and spacing of the irregularities and on the relative position towards those. This is especially critical as it was shown that dynamic soaring trajectories include a low turn as close as possible to the surface (Sachs, 2004) maintains a 1.5 m ground clearance from the centre of gravity of the bird). So equation (6) cannot be used with a z_0 of 3 cm for characterising the wind field in the first metres above the surface.

A refined model must be approached in order to provide the roughness length z_0 of the ocean surface. Wind-waves interaction is a vast field of research far from being completely clear. Nevertheless, Charnock's roughness length model, developed by the eponym author, is a generally recognised way of relating roughness length to the wave spectrum (Fairall et al., 1996). The Charnock's relation follows in equation (7), where g is the gravity.

$$z_0 = \alpha \frac{u_*^2}{g} \tag{7}$$

Stronger shear stress induces higher irregularities, which results in a greater roughness length. The parameter α is called the Charnock's parameter and is estimated to be within the [0.01; 0.035] range. This parameter was shown to depend on the wave fetch, that is to say the length of water over which a given wind has blown. It is directly related to the wave age, but it can be assumed constant for some cases. Indeed, the Charnock's parameter $\alpha_c = 1/80$, which is then called the Charnock's constant, was shown through wind field measurements (Donelan et al., 1993) to be accurate for long fetch cases, corresponding to old waves. The use of Charnock's constant might reach some limits in coastal areas, where the surface roughness of young waves is higher than predicted. For a friction velocity of 50 cm/s, the corresponding surface roughness length obtained using

Charnock's model is 0.28 mm, which is much more consistent with the order of magnitude given by Stull (1994).

2.2 Ocean waves

The way the mean wind velocity is subsequently defined with equation (6), for a roughness length that follows Charnock's model with $\alpha = \alpha_c$, gives a model of shearing flow over a rigid ocean surface, where irregularities are taken into account statistically.

However, the ocean surface is obviously constantly moving, and so to the effect of turbulent shear flow over rigid surfaces must be added the effect of surface displacement. Besides, only small scale structures of the surface, of the order of the cm are taken into account using Charnock's model. It must be superposed an effect that accounts for larger structures, if the wind field in the vicinity of significant waves is to be modelled.

Ocean waves are stochastic; the surface appears to be composed of random waves of various lengths and periods with no simple repeating pattern. Yet, one way to model this surface is the concept of wave spectrum which distributes wave energy among different wave frequencies. This decomposition of the ocean surface into an infinite sum of independent propagating sinusoidal waves relies on the fair assumption that nonlinear interactions between waves are weak. The wave spectrum is established by measurement of the height ζ of the sea surface from a fixed location, independently of the direction of waves. Pierson and Moskowitz did such measurements at a deep-sea location in the North Atlantic and made the assumption of a fully-developed sea to propose a simple, yet commonly used Pierson-Moskowitz spectrum (Carter, 1982).

$$S_{PM}(\omega)\frac{8.1}{10^3}\frac{g^2}{\omega^5}\exp\left(\frac{-5}{4}\left\{\frac{\varepsilon_p}{\omega}\right\}^4\right) \tag{8}$$

where ω_p is the peak angular frequency of the spectrum and is expressed in terms of wind measured at 19.5 metres, $U_{19.5}$, which was the height used in experiments.

$$\omega_p = 2\pi f_p = 0.8772\frac{g}{U_{19.5}} \tag{9}$$

Such that

$$\frac{dS_{PM}}{d\omega}(\omega_p) = 0 \tag{10}$$

Assumption is going to be made that the wavy surface used in the reminder of this paper consists in a single sinusoidal wave at the peak angular frequency, as shown in Figure 2, obtained after the wind blew steadily for a long time over long distances. Wind and waves have reached equilibrium: the sea is fully-developed. The local wind considered is at the origin of the formation of the wave system so waves are propagating with a phase velocity c in the same direction as the wind. Dispersion relations follow in equations (11) to (13).

$$c = \frac{g}{\omega_p} \tag{11}$$

$$k = \frac{\omega_p^2}{g} \tag{12}$$

$$\lambda = \frac{2\pi}{k} \tag{13}$$

The equation of the surface Z_{wave} is:

$$Z_{wave} = a\cos(ky + \omega_p t) \tag{14}$$

The amplitude a of the wave is also related to the wave spectrum by assuming the peak frequency concentrates all the energy from the wave spectrum. The standard deviation in surface displacement obtained from the spectrum is expressed in equation (15).

$$\langle \zeta^2 \rangle = \int_0^\infty S_{PM}(\omega)d\omega = \frac{2.74}{10^3}\frac{U_{19.5}^4}{g^2} \tag{15}$$

For the sinusoidal peak wave expressed in equation (14), this translates into equation (16).

$$\langle Surf_{wave}^2 \rangle = \frac{a^2}{2} \tag{16}$$

So the amplitude considered is given in equation (17).

$$a = \sqrt{2\int_0^\infty S_{PM}(\omega)d\omega} = \frac{7.42}{10^2}\frac{U_{19.5}^2}{g} \tag{17}$$

The wave considered is therefore highly dependent on wind conditions, as both amplitude and frequency are linked with the nominal wind speed. It should be noted, by combining equation (9) and equation (11) into equation (18), that the wave travels faster than the wind, as noted by Pierson and Moskowitz.

$$c = 1.14U_{19.5} \tag{18}$$

Therefore, the overall surface Z_{wave} of the wave is described by equation (14) and it is associated with a surface roughness entailed by small irregularities from the main surface. Those are only taken into account statistically following Charnock's model, as described in equation (7).

2.3 Wind field over waves

The undisturbed flow over a rather flat surface has been investigated, together with properties of a peak-frequency wave which concentrates all the energy of the wave spectrum. The remaining of this part focuses on the way the latter wave alters the wind field in its vicinity. It is to be noted that some tens of metres above the surface, the mean velocity profile would be roughly unaffected, so that $U_{19.5}$ is quasi constant, for a given friction velocity.

Figure 2 Aspect of a sinusoidal wave induced by a wind blowing in the y direction (see online version for colours)

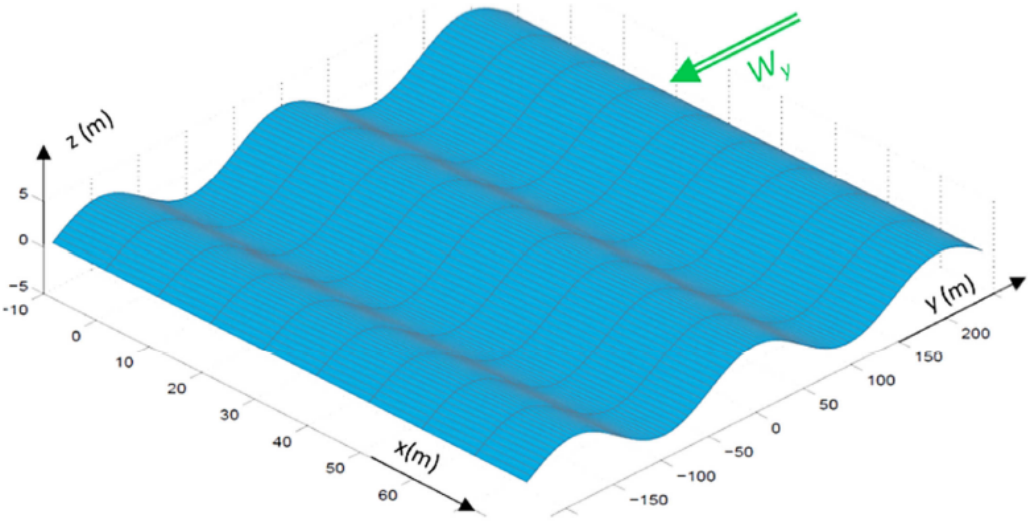

Several authors investigated the turbulent flow over such a wavy surface, using numerical simulations (Sullivan et al., 2000) or a theoretical approach (Benjamin, 1959). It was decided to use here expressions derived out of Benjamin's (1959) development which provides approximations of analytical solutions applying stable laminar flow theory. Validity of the solution only requires that the wave amplitude is small relative to the wavelength in order to remain out of flow separation cases. This condition was chosen following results from Sullivan et al. (2000) and Benjamin (1959) and is given in equation (19).

$$\frac{a}{\lambda} \leq 0.02 \; ie \; ak \leq 0.126 \tag{19}$$

In a region where there is no large adverse pressure gradient, the flow tends to follow the contour of the wave in such a way that the main features of the undisturbed boundary layer are preserved. The flow is assumed to be two dimensional in the (y, z) plane, with the wind coming from the North. The inertial reference frame $\{x_p, y_p, z_p\}$ is defined such that it translates with waves in uniform rectilinear motion at phase velocity c_p. A surface-fitted curvilinear system of coordinates (ξ, η) is defined as in equation (20), from the set of Cartesian coordinates (y_p, z_p).

$$\begin{cases} \xi = y_p - iae^{-k(z_p - iy_p)} \\ \eta = z_p - ae^{-k(z_p - iy_p)} \end{cases} \tag{20}$$

Only the real part of equation (20b) is to be considered.

$$\begin{cases} \xi = y_p - a\sin(ky_p)e^{-kz_p} \\ \eta = z_p - a\cos(ky_p)e^{-kz_p} \end{cases} \tag{20b}$$

It should be observed that the equation of Z_{wave} in the inertial frame of reference $\{x_p, y_p, z_p\}$ is given by $\eta = 0$, to the first order in ak. Periodical variations of ξ and η with y_p and z_p are damped by the exponential term in $-kz_p$. Hence, far away from the surface, the curvilinear coordinates fits with the Cartesian system and the influence of the wave decays.

The undisturbed mean velocity profile is transformed into curvilinear coordinates to follow the contour of the wave so that it varies with η only.

$$\bar{u} = \bar{u}(\eta) = \frac{u_*}{\chi}\log\left(\frac{\eta}{z_0}\right) \tag{21}$$

In the absence of waves, the stream function ψ_0 is expressed in equation (22).

$$\psi_0 = \int_0^{\eta} \{\bar{u} - c\} d\eta \tag{22}$$

For the disturbed flow, a periodic perturbation is introduced to ψ_0.

$$\psi = \psi_0 + a\left\{F(\eta) + \{\bar{u} - c\}e^{-k\eta}\right\}e^{ik\xi} \tag{23}$$

where F is a perturbation velocity that must be determined. Components of the velocity expressed in the orthonormal base of vectors linked to the curvilinear coordinates are expressed in equation (24).

$$\begin{cases} U(\eta, \xi) = J^{1/2}\dfrac{\partial\psi}{\partial\eta} \\ V(\eta, \xi) = -J^{1/2}\dfrac{\partial\psi}{\partial\xi} \end{cases} \tag{24}$$

where J is the Jacobian of the transformation given in equation (25).

$$J = \left\{\frac{\partial\xi}{\partial y_p}\right\}^2 + \left\{\frac{\partial\xi}{\partial z_p}\right\}^2 \tag{25}$$

The set of velocity components (U, V) abides by non-slipping boundary conditions at the surface of the wave.

$$\begin{cases} U(0, \xi) = -c \\ V(0, \xi) = 0 \end{cases} \tag{26}$$

Figure 3 Streamlines, pictured in a 2D plane, viewed from a reference frame translating at wave celerity (see online version for colours)

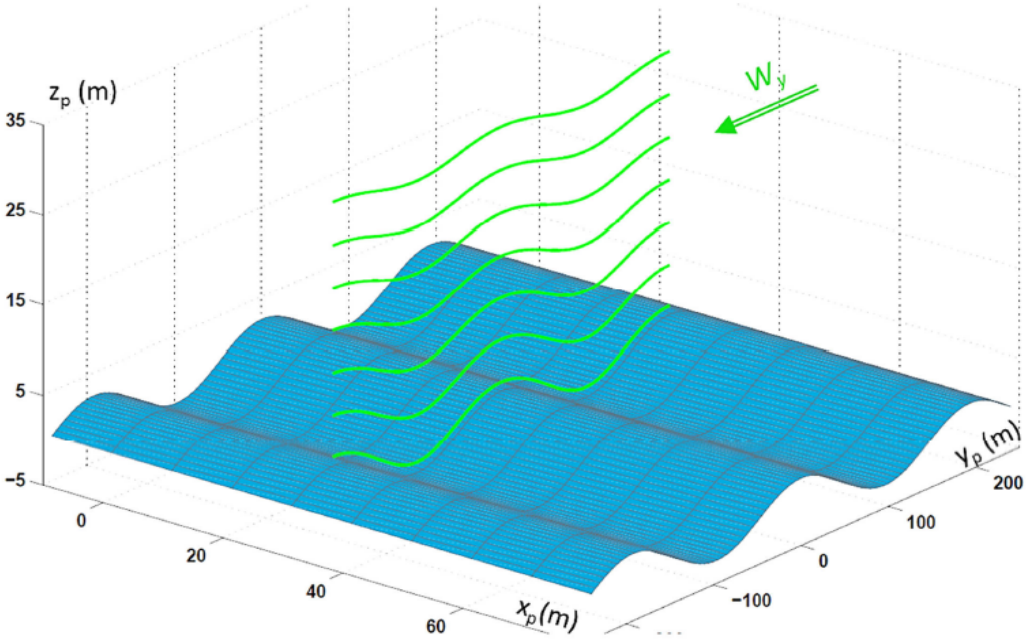

Benjamin (1959) decomposes F in an inviscid solution Φ completed with a rapid varying solution f which is a valid approximation of F close to the surface, where viscosity prevails. The region where f is significant is only several times the friction length, to the order of the millimetre. It was chosen to ignore that contribution that would have no incidence on the flight dynamics. The following approximation for F was chosen.

$$F = \Phi = -\{\bar{u} - c\}\, e^{-k\eta} \tag{27}$$

Such that

$$\begin{cases} U(\eta, \xi) = J^{1/2}\{\bar{u} - c\} \\ V(\eta, \xi) = 0 \end{cases} \tag{28}$$

The ξ-lines are thus streamlines according to this approximation, as visualised in Figure 3, and the wave influence on the streamlines decays with altitude.

Benjamin concludes that a fair approximation to the flow pattern is obtained simply by bending the primary profile.

The transformation into Cartesian coordinates $\{x_p, y_p, z_p\}$ gives the respective components of the velocity parallel to y_p and z_p.

$$\begin{cases} W_{y_p} = \dfrac{U(\eta, \xi)}{J^{1/2}} \dfrac{\partial \xi}{\partial y_p} = \{\bar{u} - c\} \dfrac{\partial \xi}{\partial y_p} \\ W_{z_p} = \dfrac{U(\eta, \xi)}{J^{1/2}} \dfrac{\partial \xi}{\partial z_p} = \{\bar{u} - c\} \dfrac{\partial \xi}{\partial z_p} \end{cases} \tag{29}$$

Finally, in the Earth's reference frame, the wind field is described by equations (30) to (34).

$$\begin{cases} W_y = W_y^{bend} + W_y^{orbital} \\ W_y = W_z^{bend} + W_z^{orbital} \end{cases} \tag{30}$$

$$W_y^{bent} = -\bar{u}\left\{1 + ake^{-kz}\cos\left(ky + \omega_p t\right)\right\} \tag{31}$$

$$W_z^{bend} = \bar{u}\left\{ake^{-kz}\sin\left(ky + \omega_p t\right)\right\} \tag{32}$$

$$W_z^{orbital} = c\left\{ake^{-kz}\cos\left(ky + \omega_p t\right)\right\} \tag{33}$$

$$W_z^{orbital} = -c\left\{ake^{-kz}\sin\left(ky + \omega_p t\right)\right\} \tag{34}$$

The superposition of two contributions can be observed. One comes from the main velocity profile being 'bent' to follow the curve of the wave, see Figure 4(a). Equation (31) is applied successively at the wave crest and at the wave trough in equations (35) to (36), in order to get an understanding of the contribution of the bent profile on the horizontal component of the wind speed.

$$W_y^{bent}(wave\ crest) = -\bar{u}\{1 + ake^{-kz}\} \tag{35}$$

$$W_y^{bent}(wave\ trough) = -\bar{u}\{1 - ake^{-kz}\} \tag{36}$$

This contribution sees a speed up at wave crest and a slow down at wave trough, as expressed by equations (35) to (36).

Moreover, this bent wind field also induces an upward deflection of the wind on the windward side of the wave and a downward deflection on the leeward side, in a wind-over-hill fashion, as can be seen in Figure 4(a).

Figure 4 (a) Velocity profiles of the wind component due to the wave curvature* (b) Velocity profiles of the wind component entailed by the orbital motion of the wave** (c) Velocity profiles of the wind established over a moving wavy surface (see online version for colours)

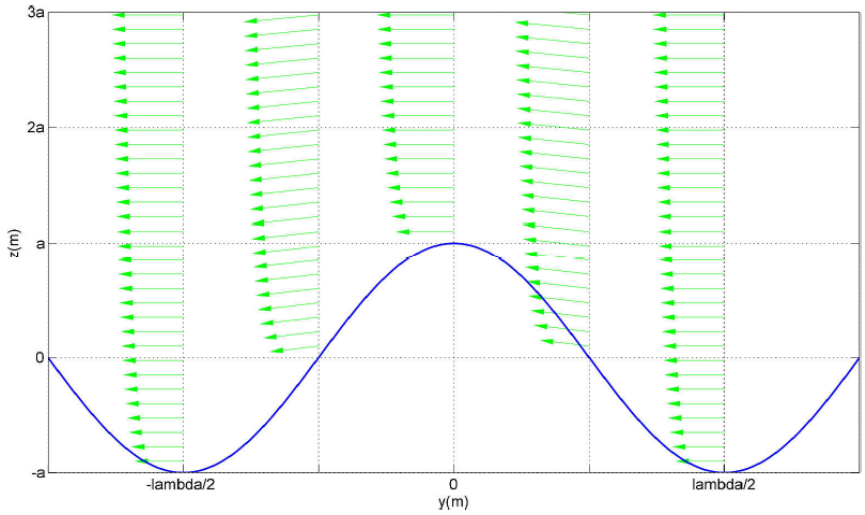

(a)

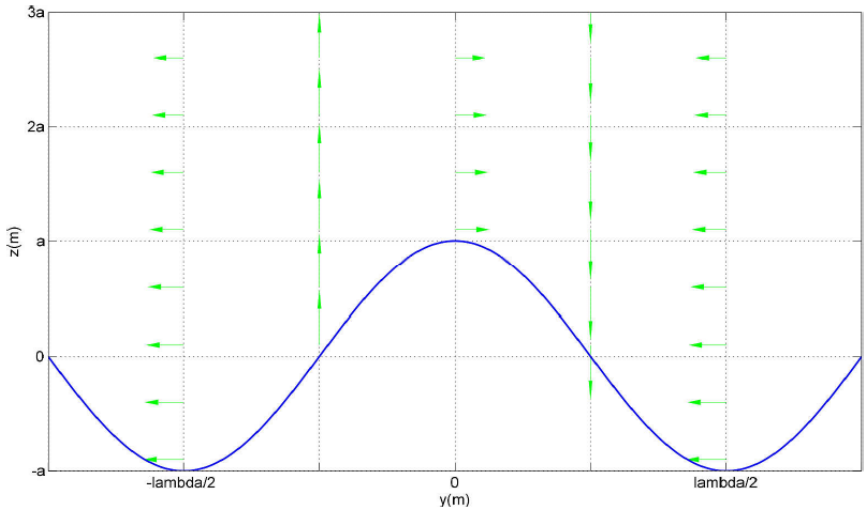

(b)

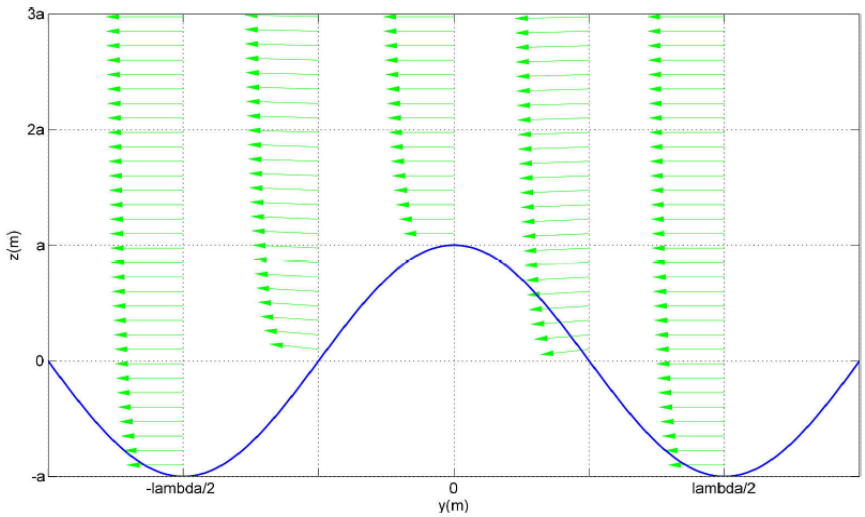

(c)

Notes: *The vertical amplitude scale of the wave is voluntarily exaggerated. **The velocity scale is five time that of Figure 4(a).

The second contribution is entailed by the orbital motion of the wave surface, with perturbations opposite to those due to the 'bent' profile, see Figure 4(b). Indeed, the moving wave creates an upward motion of the surface on the forward moving side which is the leeward face of the wave, where the 'bent' profile creates a downdraft component.

An opposite behaviour between 'orbital' and 'bent' contributions can also be observed on the other face of the wave, windward.

It is to be noted, from equation (30) and equation (34), that wherever the celerity c of the wave exceeds the local mean wind speed $\overline{u}$, the orbital vertical contribution is predominant. Therefore, the overall wind field sees an updraft on the leeward face of the wave, as can be seen in Figure 4(c).

3 Flight mechanics

3.1 Vehicle model

A point mass model is used to describe the vehicle. That is to say all forces are concentrated at the centre of gravity G and inertias are not taken into account. As dynamic soaring flight is directly inspired by the flight of albatrosses, the vehicle was given the properties of the *wandering albatross* for the sake of validation and comparison with previous studies.

Figure 5 Overall aspects of a wandering albatross, in comparison with a common Pigeon (see online version for colours)

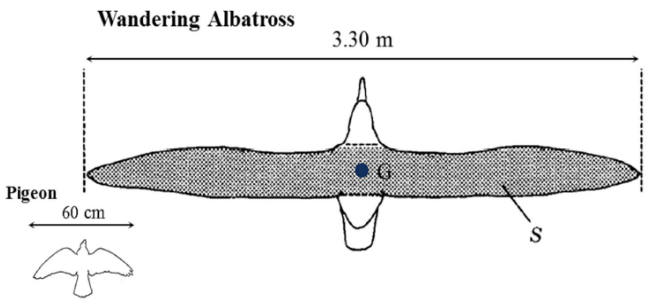

Table 1 Physical characteristics of the vehicle

Mass	8.5 kg
Wing span	3.3 m
Wing area	0.65 m^2
Aspect ratio	16.8
(C_L/C_D)max	20
$\{C_{D0}; C_{D2}\}$	$\{0.033; 1/(\pi AR\}$
C_{Lmax}	1.5

Sachs has come to an estimate about the possible characteristics of an albatross, based on measurements and data from different authors (Sachs, 2004). This model has been used several times for numerical studies and is therefore a good support for validation. Characteristics of the bird that were chosen for the vehicle model are summed up in Table 1.

3.2 Equations of motion

The motion of the point-mass model is described by the evolution of state variables, which is governed by the state of the system itself and by variations of control variables: the bank angle ϕ and the coefficient of lift C_L. Among state variables, V_i is the inertial speed, ψ_i is the inertial azimuth angle measured positively from the North to the East, γ_i is the inertial flight path angle measured positively when the vehicle climbs, while $\{x, y, z\}$ is the set of earth-relative Cartesian coordinates oriented respectively towards North, East and downwards. Identical notations are used as for air relative variables with the subscript *air* used rather than *i*. Other notations refer to S for the wing area.

Lift and drag are referred as L and D and are expressed as in equations (37) to (38).

$$L = \tfrac{1}{2}\rho.S.C_L.V_{air}^2 \tag{37}$$

$$D = \tfrac{1}{2}\rho.S.\left(C_{D0} + C_{D2}.C_L^2\right).V_{air}^2 \tag{38}$$

Contributions from lift, drag and weight add to form the respective forces F_x, F_y, F_z along the x, y, z axis, expressed as following.

$$\begin{aligned} F_x &= -L\left(\sin\phi\sin\psi_{air} + \cos\phi\cos\psi_{air}\sin\gamma_{air}\right) \\ &\quad -D\cos\gamma_{air}\cos\psi_{air} \end{aligned} \tag{39}$$

$$\begin{aligned} F_y &= L\left(\sin\phi\cos\psi_{air} - \cos\phi\sin\psi_{air}\sin\gamma_{air}\right) \\ &\quad -D\cos\gamma_{air}\sin\psi_{air} \end{aligned} \tag{40}$$

$$F_z = -L\cos\phi\cos\gamma_{air} + D\cos\gamma_{air} + mg \tag{41}$$

The set of equations of motion which govern the evolution of state variables over time is detailed in equations (42) to (47).

$$m\dot{V}_i = F_x\cos\gamma_i\cos\psi_i + F_y\cos\gamma_i\sin\psi_i - F_z\sin\gamma_i \tag{42}$$

$$mV_i\cos\gamma_i\dot{\psi}_i = -F_x\sin\psi_i + F_y\cos\psi_i \tag{43}$$

$$-mV_i\dot{\gamma}_i = F_x\sin\gamma_i\cos\psi_i + F_y\sin\gamma_i\sin\psi_i + F_z\cos\gamma_i \tag{44}$$

$$\dot{x} = V_i\cos\gamma_i\cos\psi_i \tag{45}$$

$$\dot{y} = V_i\cos\gamma_i\sin\psi_i \tag{46}$$

$$\dot{z} = -V_i\sin\gamma_i \tag{47}$$

3.3 Optimisation problem

Equations (42) to (47) accept an infinite range of solutions since control variables can pilot the evolution of the system in so many different ways. An efficient way to find out the set of control variables that would produce an energy-extracting trajectory is to solve an optimisation problem. From a basic knowledge of dynamic soaring principles that will help to set an initial guess for variables,

the optimisation would find the particular trajectory that maximises or minimises an objective function while abiding by a set of constraints.

The objective function in this case would be to minimise u_* required to perform an energy-neutral cycle of trajectory. It is to be noted that energy is defined with respect to the earth inertial reference frame. A set of constraints completes the problem. First of all, the energy-extraction should be assessed between two comparable states of the system. The trajectory should therefore include periodicity requirements on some of, if not all, the six state variables. Then, certain operational limitations need to be taken into account, such as imposing a wing tip clearance above the water and avoiding stall. Equations of motion are taken into account as constraints and initial conditions must be specified.

The underlying nonlinear constrained optimisation problem is expressed in a discretised time interval using collocation techniques (Hull, 1997). Indeed, the infinite dimension problem is converted into a parameterised problem by discretising the solution time history into a number of intervals, which will be of constant length dt here.

The state variable evolution with time, stated in equations (42) to (47), is approximated over each interval using interpolation techniques at some well-defined interpolation points, called collocation points. The equations of motion are then verified over each interval by bringing a residual to zero as part of the optimisation process.

This translates by using in this case fourth-order Simpson one-third rule with a Hermitecubic polynomial that interpolates the evolution of state variables over each interval. Equations of motion are then satisfied at the midpoint of each interval by bringing the residual expressed in equation (50) to zero. The integration of equations of motion is therefore part of the optimisation process. In this implicit integration scheme, the solver iterates on both state and control variables to reach an optimum. So for the vector of state variables $\boldsymbol{X}$, the vector of control variables $\boldsymbol{u}$, the vector function g representing the equations of motion, over a time interval of length dt between collocation points k and $k + 1$, the state variables are evaluated at midpoint of each interval as $\boldsymbol{X_m}$ in equation (48) and the control variables as $\boldsymbol{u_m}$ in equation (49).

$$\boldsymbol{X_m} = \frac{\boldsymbol{X_k} + \boldsymbol{X_{k+1}}}{2} - \frac{1}{8} \cdot \left[g\left(\boldsymbol{X_{k+1}}, \boldsymbol{u_{k+1}}\right) - g\left(\boldsymbol{X_k}, \boldsymbol{u_k}\right) \right].dt \tag{48}$$

$$\boldsymbol{u_m} = \frac{\boldsymbol{u_k} + \boldsymbol{u_{k+1}}}{2} \tag{49}$$

For each state variable X^i amongst $\{X^1, X^2, \ldots, X^6\}$,the scalar residual R_k^i is expressed at collocation points k as in equation (50).

$$R_k^i = X_{k+1}^i - X_k^i - \frac{1}{6} \cdot \left[g^i\left(\boldsymbol{X_k}, \boldsymbol{u_k}\right) + 4.g^i\left(\boldsymbol{X_m}, \boldsymbol{u_m}\right) + g^i\left(\boldsymbol{X_{k+1}}, \boldsymbol{u_{k+1}}\right) \right].dt \tag{50}$$

This is a nonlinear constrained optimisation problem. The residual at collocation point k is a function of state variables at k and $k + 1$ only, so the Jacobian matrix relative to the problem is sparse. The solver SNOPT (Gill et al., 2005) is appropriate for this type of problem and was chosen to find an optimum.

For the case with waves, periodicity constraints do not affect the absolute position of the vehicle anymore but its position relative to the wave. So the vehicle starts and stops at the same position towards the wave, and this only affects y as the wave travels in that direction. In order to satisfy convergence, once the initial y-position towards the wave is chosen, the amplitude is gradually increased from a flat-surface case. The case is assumed to be physical when the amplitude reaches the value calculated with the wave spectrum theory, defined in equation (17).

4 Dynamic soaring cycle

One computation is made with an optimisation problem matching the case from Sachs (2004), in order to validate the optimisation methodology as well as provide a classical study case of dynamic soaring over a flat surface. All vehicle properties, environment conditions and optimisation constraints mentioned by Sachs are reproduced here. The minimal altitude was set to 1.5 m, the maximal load factor to 3, the surface roughness length is 3 cm, the vehicle is that of Table 1 and the bank angle is limited to 80°. The energy-neutral cycle described in Figure 6, is obtained by minimising the friction velocity required to perform the neutral cycle without any power input from the vehicle.

Overall results match very well the simulation made by Sachs, as can be compared in Table 2. Some minor disparities can be explained by differences in the methodology between Sachs' simulation and the present one. Indeed, some practical aspects, such as for instance the number of time discretisation nodes or the selected integration scheme are not specified in Sachs' publication and therefore probably differ between the two. Results obtained match Sachs' by less than 5%, hence, validating the methodology set in the case of dynamic soaring over a rather flat surface with a 3 cm roughness length.

Table 2 Comparison between simulations obtained by Sachs (2004) and in the current paper

	Sachs	*Current*	*Relative disparity*
t_f (s)	7.2	7.0	2.8%
u_* (cm.s^{-1})	60.7	60.6	0.2%
Max. height (m)	20.5	20.1	2.0%
Eastern net speed (m.s^{-1})	9.37	9.38	0.1%
Eastern period (m)	66.5	65.8	1.1%

Figure 6 Optimised energy-neutral open trajectory for condition representing Sachs (2004) (see online version for colours)

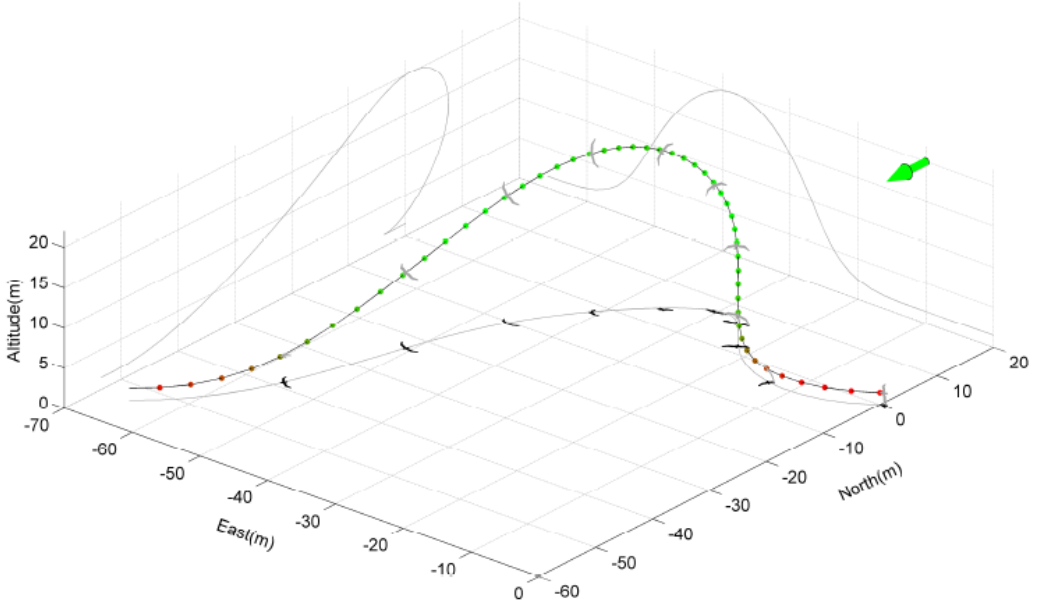

Note: The simulation is obtained for a rather flat surface of 3 cm-roughness. The wind friction velocity required to sustain dynamic soaring flight is 60.6 cm/s, the time duration is 7 s.

The trajectory exposed in Figure 6 shows a typical dynamic soaring trajectory. The wind direction is shown by the green arrow, coming from the North direction. Along the path, dots are coloured whether the vehicle sees energy gain (green) or loss (red). Four typical segments can be identified. One climb upwind is followed by the upper turn in the direction of the wind. Then a descent downwind begins before a low turn into the wind, close to the surface. Variations in total energy along the path depend on the work of aerodynamic forces that are deflected from inertial directions by the presence of wind, as it is explained by Bonnin et al. (2013). As can be seen by the colour of dots along the path, the energy extraction is periodic, with gains during the climb, the upper turn and the dive. Those are offset by losses during the lower turn, hence highlighting the necessity to fly close to the surface during the turn into the wind, to cope with the lowest wind strength. Overall, the vehicle travels in a net direction angled from the wind direction, managing to travel eastward but being carried away by the wind in the process.

5 Ocean dynamic soaring

In order to take waves and the induced wind field into account, the amplitude a was increased manually and given as an input to the solver, which then worked on minimising u_*, in an environment with travelling waves of amplitude a and angular frequency $\omega_p(u_*)$, as well as roughness length $z_0(u_*)$.The amplitude a was then compared with the theoretical amplitude of the peak wave, see equation (17), and adjusted. The process was eventually repeated until the two amplitudes were identical, hence simulating fully-developed waves under winds blowing at u_*.

5.1 Realistic roughness

A first case without amplitude was run, with a surface correlated to wind conditions only through the roughness length. The wind friction velocity required was u_* of 0.65 m/s, with a corresponding roughness length z_0 of 0.48 mm and a reference wind speed at 10 metres of 15.8 m/s. Those values strongly differ from the validation case, as the roughness length is calculated using Charnock's model and not fixed at 3 cm anymore. It can be argued that the roughness length could be higher than 0.48 mm, as a rather flat surface of a non-developed sea under recent winds has a higher roughness than old waves.

Figure 7 From top to bottom, change in periodicity

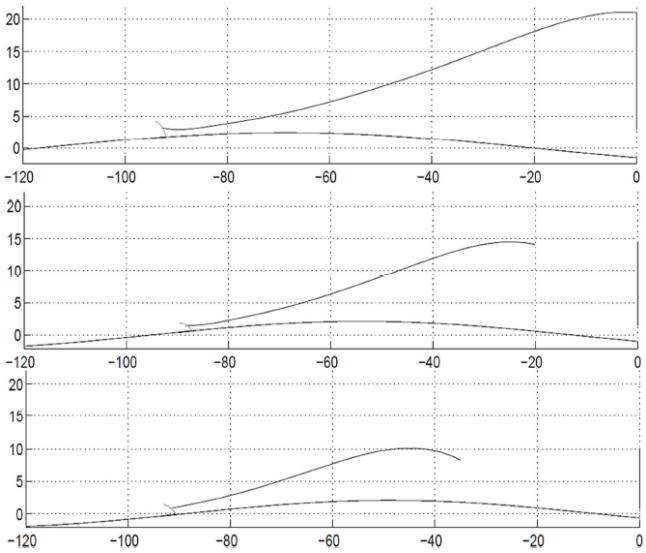

Notes: a (m); u_* (m/s)} = {2.47; 0.57}; {2.25; 0.53}; {2.05; 0.51}.

Figure 8 Evolution of the vehicle and wave with time (see online version for colours)

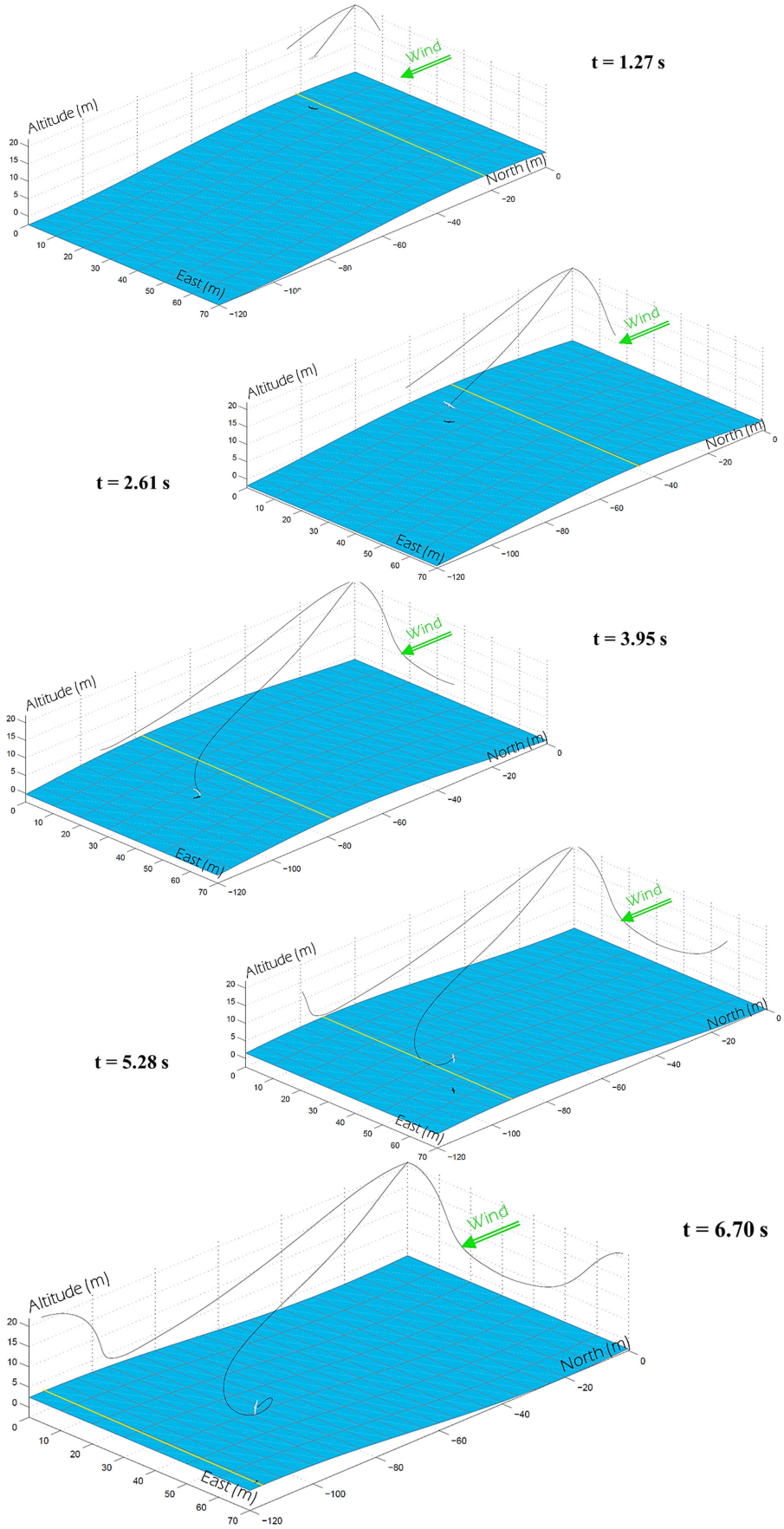

Notes: u_* = 0.57 m/s; a = 2.47 m; λ = 193 m; c = 17.5 m/s.

The wind required to sustain dynamic soaring flight is much higher than initially computed. This highlights the significance of the roughness length as for dynamic soaring performances and confirms the need for improvements from the first dynamic soaring simulations.

5.2 Moving wavy surface

In Figure 8, the vehicle arbitrary starts (t = 0) and stops (t = 6.70 s) above the crest of the wave. It can be seen that the vehicle gains ground towards the wave during the descent downwind (t = 2.61 s). Hence, it begins the lower turn close to the surface (t = 3.95 s) ahead of the crest, on the forward face of the moving wave (the leeward side from a wind point of view). A wing tip clearance of 5 cm is imposed. Then, the same type of climb upwind and upper turn as before are observed.

Although the net speed in the y-direction is imposed to be the same as the wave celerity c, the vehicle is 'free' to manoeuvre between initial and final positions above the crest. Besides, it is observed during the convergence iteration process, when the amplitude is slightly increased step by step, that those changes are affecting both the trajectory and the minimal friction velocity required. The case without waves sees a friction velocity of 0.65 m/s whereas the presence of waves enables to achieve a cycle for u_* = 0.57 m/s. The vehicle is therefore getting benefits from the presence of the wave, by flying on the forward side which sees a local wind updraft, during the lower turn close to the surface. Although this contribution is not sufficient to balance drag losses and therefore to gain energy, it can be compared as a superposition of wind-gradient soaring with slope soaring, where the slope would be a travelling wave. Increasing the ratio a/l would increase the latter effect.

Results from Figure 7 are obtained by displacing the initial/final position of the vehicle forward relative to the wave, rather than at the crest, therefore allowing it to spend a greater fraction of the trajectory in the location of local wind updraft. It shows that the required wind strength is lowered as well as the wind-related amplitude. Besides, as losses during the lower turn are decreased, the vehicle does not need to climb as much as before, and the maximal height reduces from 20 metres down to 15 and lower, in better accordance with on-the-field observations of albatrosses (Pennycuick, 2002).

6 Conclusions

This paper presents a refinement in the theory of ocean dynamic soaring by taking into account of waves. It completes dynamic soaring studies by stepping a bit further towards a realistic model and therefore aims at investigating further the feasibility to exploit dynamics soaring for engineering applications.

It is first shown that adopting a constant 3 cm roughness length is not particularly adapted in the case of low-level flight above waves. A particular care is given to explicit the methodology used to model the environment. The ocean surface roughness is adapted by using a well-known, and validated, Charnock's model. Then a peak sinusoidal wave concentrating in one frequency all the energy from the Pierson-Moskowitz spectrum is defined. By considering quite shallow wave trains, stable laminar theory can be applied to determine the induced wind field, therefore, ignoring turbulent interactions between wind and wave. Finally, an optimisation routine is applied to the point mass model albatross so as to derive an energy neutral trajectory cycle.

It is shown that the upward deflection of the wind field on the forward face of the wave due the orbital motion can be exploited by the vehicle during the lower turn into the wind in order to minimise losses characteristic to this segment. The consequence is to lower the wind strength required to perform such an energy neutral cycle. Finally, it is shown quite intuitively that allowing the vehicle, by changing periodicity constraints, to fly for a longer part of the trajectory on the forward face of the wave has a positive impact energy-wise, even though the reference wind required is still high compared to observations (Sachs et al., 2011).

The point mass model used in this paper is a 3 degree of freedom model, although the bank angle and the pitch angle are somehow indirectly piloted. The use of a more complex flight mechanics model, extended to 6 degree of freedom, could be interesting to enhance the comprehension of the albatross flight. It would anyway be a necessary step forward if the problem is to be approached from a control perspective. However, the complexity of the optimisation procedure will certainly increase.

Further refinements from the environment model can potentially introduce other favourable conditions to dynamic soaring. As such, younger and rougher waves could play an important role as well as a refined shape of the wave with higher crests and deeper thoughts. Eventually, flow separation could be considered to question the benefits of performing the lower turn inside the recirculation zone.

Acknowledgements

This PhD is financed by the French Direction Générale de l'Armement (DGA) under a dual DGA/DSTL agreement to sponsor joint French/UK PhDs.

References

Barate, R., Doncieux, S. and Meyer, J-A. (2006) 'Design of a bio-inspired controller for dynamic soaring in a simulated UAV', *Bioinspir. Biomim.*, Vol. 1, No. 3, pp.76–88.

Benjamin, T.B. (1959) 'Shearing flow over a wavy boundary', *Fluid. Mech.*, Vol. 6, No. 2, pp.161–205.

Bonnin, V., Toomer, C. and Benard, E. (2013) 'Energy harvesting mechanisms for UAV flight by dynamic soaring', *AIAA AFM Conference*, Boston, AIAA 2013-4841, August.

Bower, G.C. (2011) *Boundary Layer Dynamic Soaring for Autonomous Aircraft: Design and Validation*, PhD dissertation, Aeronautics and Astronautics Dept., Stanford, December.

Carter, D.J.T. (1982) 'Prediction of wave height and period for a constant wind velocity using the JONSWAP results', *Ocean Eng*., Vol. 9, No. 1, pp.17–33.

Deittert, M., Richards, A., Toomer, C. and Pipe, A. (2009) 'Engineless unmanned aerial vehicle propulsion by dynamic soaring', *J. Guid. Cont. Dyn*., Vol. 32, No. 5, pp.1446–1454.

Donelan, M., Dobson, F.W., Smith, S.D. and Anderson, R.J. (1993) 'On the dependence of sea surface roughness on wave development', *Journal of Phys. Ocean*., September, Vol. 23, No. 9, pp.2143–2149.

Fairall, C.W., Grachev, A.A., Bedard, A.J. and Nishiyama, R.T. (1996) *Wind, Wave, Stress, and Surface Roughness Relationships from Turbulence Measurements Made on R/P Flip in the Scope Experiment*, A Report for the DoD ASAP Program, April.

Gill, P., Murray, M. and Saunders, M. (2005) 'SNOPT: an SQP algorithm for large-scale constrained optimization', SIAM Rev. Vol. 47, No. 1, pp.99–131.

Hull, D. (1997) 'Conversion of optimal control problem into parameter optimization problems', *J. Guid. Cont. Dyn*., January–February, Vol. 20, No. 1, pp.57–60.

Idrac, P. (1925) 'Etude expérimentale et analytique du vol sans battements des oiseaux voiliers des mers australes, de l'Albatross en particulier', *La Technique Aéronautique*, Vol. 16, No. 4, pp.9–22.

Jouventin, P. and Weimerkirsch, H. (1990) 'Satellite tracking of wandering albatrosses', *Nature*, Vol. 343, No. 6260, pp.746–748.

Monin, A.S. and Yaglom, A.M. (1987) *Statistical Fluid Mechanics*, 5th printing, The MIT Press, Cambridge.

Pennycuick, C. (2002) 'Gust soaring as the basis for the flight of albatrosses and petrels', *Avian Science*, Vol. 2, No. 1, pp.1–12.

Rayleigh, L. (1883) 'The soaring of birds', *Nature*, April, Vol. 27, No. 701, pp.534–535.

Richardson, P.L. (2011) 'How do albatrosses fly around the world without flapping their wings?', *Progress in Oceanography*, Vol. 88, Nos. 1–4, pp.46–58.

Sachs, G. (2004) 'Minimum shear wind strength required for dynamic soaring of albatrosses', *Ibis*, Vol. 147, No. 1, pp.1–10.

Sachs, G., Traugott, J. and Holzapfel, H. (2011) 'Progress against the wind with dynamic soaring results from in-flight measurement of albatrosses', *AIAA GNC Conference*, AIAA 2011-6225.

Stull, R.B. (1994) *An Introduction to Boundary Layer Meteorology*, Atmospheric Science Library, Dordrecht, The Netherlands.

Sullivan, P., McWilliams, J. and Moeng, C-H. (2000) 'Simulation of turbulent flow over idealized water waves', *J. Fluid. Mech*. Vol. 404, No. 1, pp.47–85.

US Department of Defense (2005) *Unmanned Aircraft Systems Road Map 2005–2030*, July, p.51.

Wood, C.J. (1925) The flight of albatrosses (a computer simulation)', *Ibis*, Vol. 115, No. 2, pp.244–256.

Zhao, Y. (2004) 'Minimal fuel powered dynamic soaring of unmanned aerial vehicle utilizing wind gradients', *Optim. Control. Appl. Meth*., Vol. 25, No. 5, pp.211–233.